Article

Halogen-Doped Chevrel Phase Janus Monolayers for Photocatalytic Water Splitting

Ekaterina V. Sukhanova [1,*] , **Nursultan E. Sagatov** [2] , **Aleksandr S. Oreshonkov** [1,3,4] , **Pavel N. Gavryushkin** [1,2,5] **and Zakhar I. Popov** [1,*]

1   Laboratory of Acoustic Microscopy, Emanuel Institute of Biochemical Physics of Russian Academy of Sciences, 119334 Moscow, Russia
2   Laboratory of Phase Transformations and State Diagrams of the Earth's Matter at High Pressures, Sobolev Institute of Geology and Mineralogy, Siberian Branch of Russian Academy of Sciences, 630090 Novosibirsk, Russia
3   Laboratory of Molecular Spectroscopy, Kirensky Institute of Physics, Federal Research Center KSC SB RAS, 660036 Krasnoyarsk, Russia
4   School of Engineering and Construction, Siberian Federal University, 660041 Krasnoyarsk, Russia
5   Geology Geophysics Department, Novosibirsk State University, 630090 Novosibirsk, Russia
*   Correspondence: yekaterina.sukhanova@phystech.edu (E.V.S.); zipcool@bk.ru (Z.I.P.)

Abstract: Chevrel non-van der Waals crystals are promising candidates for the fabrication of novel 2D materials due to their versatile crystal structure formed by covalently bonded (Mo_6X_8) clusters (X–chalcogen atom). Here, we present a comprehensive theoretical study of the stability and properties of Mo-based Janus 2D structures with Chevrel structures consisting of chalcogen and halogen atoms via density functional theory calculations. Based on the analysis performed, we determined that the $S_2Mo_3I_2$ monolayer is the most promising structure for overall photocatalytic water-splitting application due to its appropriate band alignment and its ability to absorb visible light. The modulated Raman spectra for the representative structures can serve as a blueprint for future experimental verification of the proposed structures.

Keywords: TMDs; non-van der Waals monolayers; Mo6S8; Mo3S4; 2D materials; exfoliation; OER; HER; nanomaterials

1. Introduction

For the most part, the investigation of two-dimensional structures is focused on the materials obtained from layered crystals such as graphite, hexagonal boron nitride (h-BN), or transition metal dichalcogenides (TMDs). The main feature of these crystals is a weak van der Waals interaction between the layers, making it possible to easily cleave them into monolayers [1]. Reducing the dimension of the material leads to the appearance of unique new properties. For example, 2D nanomaterials are usually characterized by higher values of carrier mobility and conductivity in comparison with bulk crystals due to changes in electronic properties caused by the quantum confinement effect. Therefore, the search, investigation, and fabrication of new 2D nanomaterials from non-van der Waals crystals has attracted enormous attention [2]. Bulk materials, such as iron pyrite [3] and α-germanium [3], have relatively weak covalent bonds and can be exfoliated. Moreover, the achievements in liquid-phase exfoliation techniques have led to the rapid development of a second approach to 2D materials' fabrication, which is the cleaving of non-van der Waals bulk materials into individual monolayers [2]. The successful application of this approach has led to the expansion of the 2D nanomaterials family and the fabrication of stable and easily processable nanomaterials [2].

In the 2D form, the TMDs are widely represented by MX_2 stoichiometry, where M = Mo, V, W and X = S, Se, Te. In this stoichiometry, multiple phases have been experimentally observed—the hexagonal H phase and the tetragonal T and T' (or Td) phases,

which exhibited completely different electronic properties: in the case of MoS_2, the H phase is a semiconductor, while the T phases are metals. Furthermore, several metastable TMD phases have been theoretically proposed, among which are the square-octagonal (S) and disordered square-octagonal (S') monolayers [4], another hexagonal H' phase [5], and a triclinic-structured A' phase [6,7]. Moreover, several non-stoichiometric monolayers in the M-X system have been proposed [8–11] and some of them successfully fabricated [12,13]. The above indicate the prospects of the search for and investigation of new monolayer structures in the M-X systems that can be produced from non-van der Waals crystals.

The ternary molybdenum chalcogenides, or the Chevrel phases [14], are the non-van der Waals crystals of molybdenum chalcogenides, exhibiting compelling properties for next-generation battery materials, electrocatalysts, and other energy applications [15]. In general, Chevrel phases have a formula of $M_xMo_6X_8$ where X is a chalcogen atom (S, Se, Te) and M is a metal that can have a different valency (x varying from 0 to 4) [16]. Chevrel phases demonstrate the potential for application in battery materials [17–20], catalysts [21], thermoelectric materials [22], and superconductivity [23,24]. Binary compounds formed only by molybdenum clusters Mo_6X_8 are also interesting. In such compounds, Mo_6 octahedra are surrounded by X_8 cubes in which X atoms are located above the center of each Mo face, and such clusters are interconnected by Mo–X interactions, forming an ordered structure. Most Mo_6X_8 crystals have rhombohedral symmetry and are characterized by an $R\bar{3}$ space group [16]. A facile approach to synthesizing large-scale and high-purity Mo_6S_8 nanosheets by applying an iodine vapor transport reaction was proposed [25]. Moreover, in Chevrel phases, chalcogen atoms can be partially substituted by halogen atoms [26–29] or other chalcogen atoms [30], leading to the formation of $X_aMo_6Y_{8-a}$ structures, for example $Mo_6S_6Br_2$ [28] or $Mo_6S_{6.8}Te_{1.2}$ [30].

Recently, Janus monolayers [31–34], whose main feature is the presence of two inequivalent surfaces, have attracted significant attention due to their possible application in the photocatalytic water-splitting process [35–38], leading to the production of environmentally friendly hydrogen fuel [39,40]. The TMDs also include Janus-type monolayers [41,42], which can be obtained from the structures by replacing the chalcogen atoms of one surface with chalcogen atoms of another type [6,43–46]. Some of the proposed structures were recently successfully fabricated [41,42,47,48], resulting in intensive research into new possible Janus structures [6].

In this work, for the first time, we performed a comprehensive theoretical investigation of the stability and electronic and optical properties of novel Mo-based Janus Chevrel monolayers $X_4Mo_6Y_4$ ($X \neq Y$ = O, S, Se, Te and X = O, S, Se, Te; Y = F. Cl, Br, I) and investigated the possibility of their application in photocatalytic water splitting.

2. Materials and Methods

Structure relaxation and calculations of electronic and optical properties based on density functional theory (DFT) [49,50] were carried out by the VASP program package [51–53]. The exchange-correlation functional was calculated via generalized gradient approximation (GGA) within Perdew–Burke–Ernzerhof (PBE) parameterization [54]. The projector-augmented wave (PAW) [55] basis set technique was used. The energy cutoff of plane waves were set to be equal to 520 eV. The first Brillouin zone was sampled according to the Monkhorst–Pack scheme [56] with a k-point mesh of $8 \times 8 \times 1$. Atomic structure relaxation was carried out until the energy variation between the two steps of the electronic loop became less than 10^{-8} eV and there was less than 10^{-7} eV between ionic steps. A vacuum region of at least 15 Å was chosen to avoid an artificial interaction between structures in non-periodic directions. Phonon calculations were carried out using the PHONOPY program package [57]. Charge redistribution in all considered systems was studied using Bader charge analysis [58,59]. For the atomic structure visualization, we used VESTA software [60] (version 3.4.5).

Modeling of Raman spectra was performed within the framework of DFT [61], using GGA [62] with an exchange-correlation PBE functional [54], implemented in CASTEP

code [63]. Norm-conserving pseudopotentials were also used. The plane-wave cutoff was set to 740 eV and the k-point spacing was less than 0.05 Å^{-1} for all studied compounds. Monolayer structures were relaxed until the maximum forces became less than 0.03 eV/Å and the maximum stress was smaller than 0.05 GPa. Meanwhile, in the case of bulk Mo_6S_8, the same criteria were chosen as 0.01 eV/Å and 0.02 GPa. The tolerance for finding ground-state wavefunctions was set to 1×10^{-8} eV. Density functional perturbation theory was used for the calculation of phonon spectra at the center of the Brillouin zone and was also used for the calculation of Raman tensor components (finite displacement method [64,65]).

3. Results

The unit cell of Chevrel monolayers contains 18 Mo, 12 X, and 12 Y atoms (X = O, S, Se, Te; Y = O, S, Se, Te, F, Cl, Br, I) and consists of a single $X_4Mo_6Y_4$ cluster located at some angle to the *c* axis (see Figure 1). The cluster connects with each of the four neighboring clusters by one Mo–X and one Mo–Y bond. The optimized cell parameters for each considered chemical composition are presented in Tables 1 and 2.
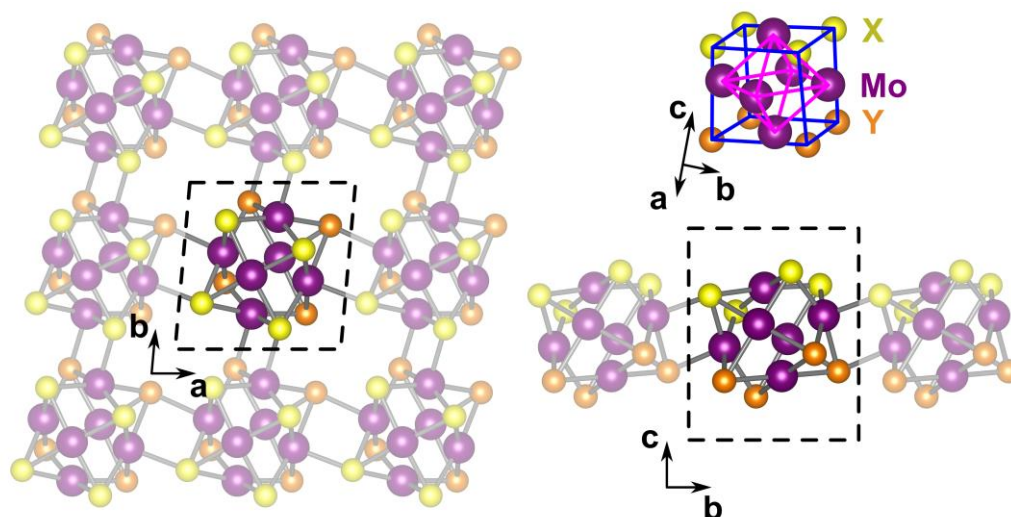
Figure 1. Atomic structure of a monolayer $X_4Mo_6Y_4$ Chevrel phase (X/Y = O, S, Se, Te or X = O, S, Se, Te; Y = F. Cl, Br, I) and a single $X_4Mo_6X_4$ cluster. The unit cell is highlighted by a black dashed line. Mo_6 octahedra and X_4Y_4 cubes are marked by purple and blue lines, respectively.

Table 1. Unit cell parameters for $Ch_2Mo_3Ch_2$ (Ch = S, Se, Te) Chevrel monolayers.

$Ch^1_2Mo_3Ch^2_2$ Monolayer	a, Å	b, Å	γ, °
$S_2Mo_3S_2$	6.518	6.623	84.89
$Se_2Mo_3Se_2$	6.644	6.738	85.10
$Te_2Mo_3Te_2$	6.834	6.902	89.73
$S_2Mo_3Se_2$	6.644	6.738	85.10
$S_2Mo_3O_2$	6.190	6.425	84.10
$S_2Mo_3Te_2$	6.834	6.902	89.73
$Se_2Mo_3O_2$	6.499	6.543	88.66
$Se_2Mo_3Te_2$	6.943	6.957	87.39
$Te_2Mo_3O_2$	6.861	7.074	90.92

Table 2. Unit cell parameters for $Ch_2Mo_3Hal_2$ (Ch = O, S, Se, Te; Hal = F, Cl, Br, I) Chevrel monolayers.

$Ch_2Mo_3Hal_2$ Monolayer	a, Å	b, Å	γ, °
$O_2Mo_3F_2$	6.148	6.131	85.87
$O_2Mo_3Cl_2$	6.362	6.286	87.38
$O_2Mo_3Br_2$	6.864	6.436	87.31
$O_2Mo_3I_2$	7.337	7.328	84.04

Table 2. *Cont.*

Ch$_2$Mo$_3$Hal$_2$ Monolayer	a, Å	b, Å	γ, °
S$_2$Mo$_3$F$_2$	6.517	6.521	86.01
S$_2$Mo$_3$Cl$_2$	6.656	6.637	86.49
S$_2$Mo$_3$Br$_2$	6.791	6.773	86.60
S$_2$Mo$_3$I$_2$	7.061	7.033	86.38
Se$_2$Mo$_3$F$_2$	6.720	6.741	85.78
Se$_2$Mo$_3$Cl$_2$	6.796	6.780	86.45
Se$_2$Mo$_3$Br$_2$	6.909	6.892	86.46
Se$_2$Mo$_3$I$_2$	7.133	7.116	86.29
Te$_2$Mo$_3$F$_2$	7.170	7.172	85.51
Te$_2$Mo$_3$Cl$_2$	7.087	7.089	86.33
Te$_2$Mo$_3$Br$_2$	7.142	7.135	86.34
Te$_2$Mo$_3$I$_2$	7.291	7.277	86.17

Chevrel monolayers can be potentially fabricated by the cleavage of corresponding bulk ternary molybdenum chalcogenides along the (110) direction for non-Janus compounds. To consider this possibility, the exfoliation energy (E_{exf}) was estimated through the equation proposed in [66]:

$$E_{exf} = \frac{E_{ML} - E_{bulk}/m}{A}$$

where E_{ML} is the total energy of a monolayer, E_{bulk} is the total energy of bulk material consisting of m monolayers (in our case $m = 1$), and A is the in-plane area according to the relaxed bulk unit cell. For the Mo$_3$S$_4$ monolayer, E_{exf} is equal to 79.54 meV/Å^2, for the Mo$_3$Se$_4$ monolayer it is 67.90 meV/Å^2, and for the Mo$_3$Te$_4$ monolayer it is 60.80 meV/Å^2. As expected, the obtained values exceed the characteristic values for Van der Waals layered crystals such as graphite (17–25 meV/Å^2) or TMDs (~50 meV/Å^2); however, the value is comparable with the estimations of the exfoliation energy for non-Van der Waals crystals [67–69] and even less than the value for experimentally exfoliated hematene [70]. Later, we divided the consideration of X$_4$Mo$_6$Y$_4$ Chevrel phases (X/Y = O, S, Se, Te or X = O, S, Se, Te; Y = F. Cl, Br, I) into two subclasses: Ch$^1_2$Mo$_3$Ch$^2_2$ (Ch^1/Ch^2 = O, S, Se, Te) and Ch$_2$Mo$_3$Hal$_2$ (Ch = O, S, Se, Te and Hal = F, Cl, Br, I) monolayers.

The dynamic stability of the two classes of Janus Chevrel monolayers—Ch$^1_2$Mo$_3$Ch$^2_2$ (Ch^1/Ch^2 = O, S, Se, Te) and Ch$_2$Mo$_3$Hal$_2$ (Ch = O, S, Se, Te and Hal = F, Cl, Br, I)—was investigated through phonon dispersion spectrum calculation. The small bulges in the vicinity of the Γ-point in the phonon dispersion spectra are known to be attributed to the lack of consideration of rotational invariance [71,72] and, therefore, not indicate the instability of the structure (see Figures 2 and 3). According to the performed analysis, we can identify that only Se$_2$Mo$_3$O$_2$ and Te$_2$Mo$_3$O$_2$ among 2D Ch$_2$Mo$_3$Ch$_2$ Janus structures and O$_2$Mo$_3$Br$_2$, O$_2$Mo$_3$I$_2$, Se$_2$Mo$_3$F$_2$, and Te$_2$Mo$_3$F$_2$ monolayers among 2D Ch$_2$Mo$_3$Hal$_2$ Janus structures fail to exhibit dynamic stability as indicated by negative (below zero) phonon dispersive energy in at least one of the X, Y, H$_1$, C, and H points of the Brillouin zone.
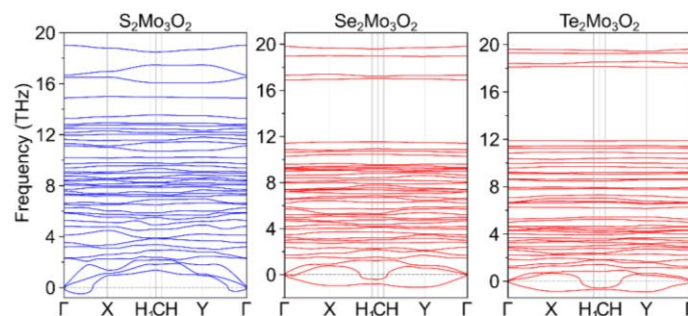

Figure 2. *Cont.*
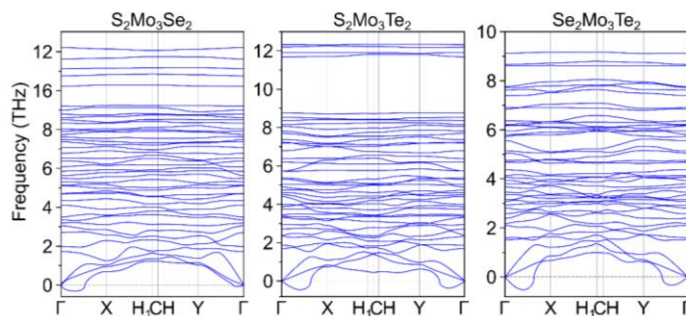
Figure 2. Phonon dispersion spectra for $Ch^1_2Mo_3Ch^2_2$ (Ch^1/Ch^2 = O, S, Se, Te) Chevrel phases.
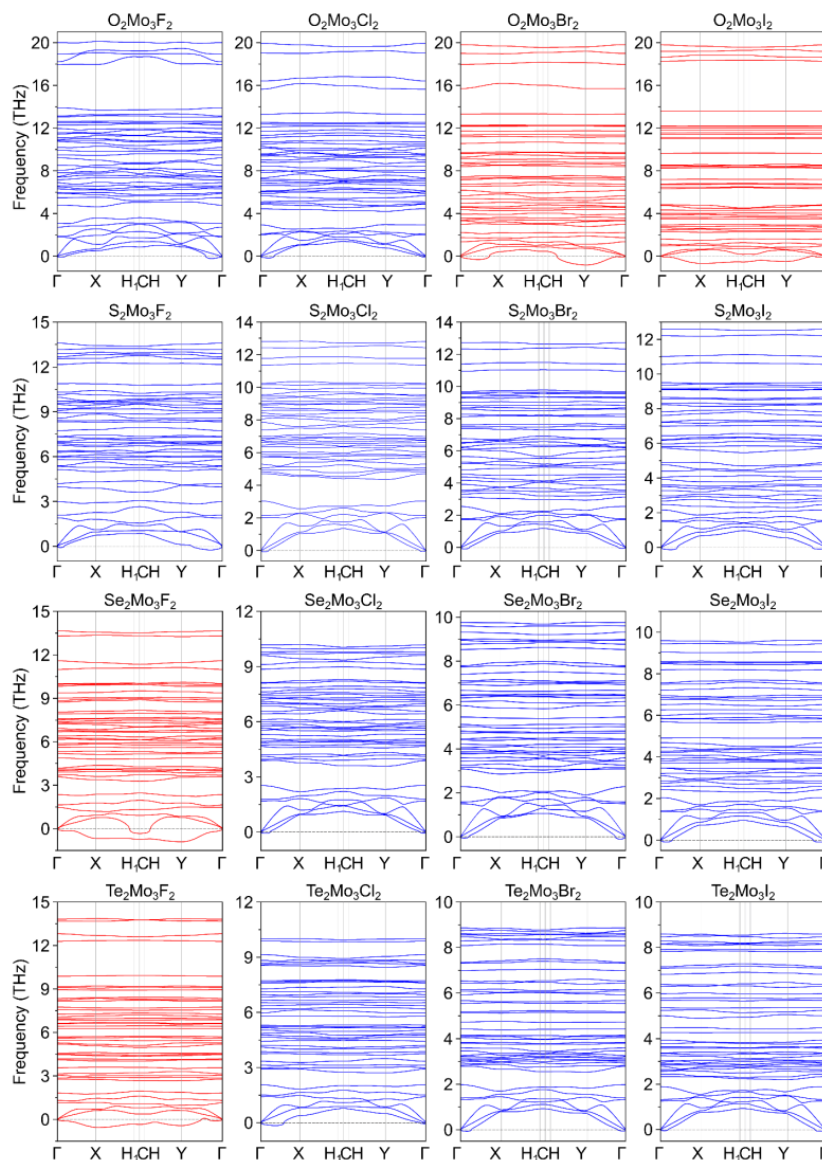
Figure 3. Phonon dispersion spectra for $Ch_2Mo_3Hal_2$ (Ch = O, S, Se, Te and Hal = F, Cl, Br, I) Chevrel phases.

We investigated the electronic properties of dynamically stable $Ch^1_2Mo_3Ch^2_2$ (Ch^1/Ch^2 = O, S, Se, Te) and $Ch_2Mo_3Hal_2$ (Ch = O, S, Se, Te and Hal = F, Cl, Br, I) monolayers. Non-Janus Mo_3S_4 Chevrel monolayers exhibit semiconducting properties with a band gap value of ~0.2 eV, while Mo_3Te_4 monolayers are metals (see Figure S2). Electronic band structures for the considered Janus monolayers are presented in Figures 4 and 5.

The substitution of chalcogen atoms on one side of the Chevrel non-Janus monolayer leads to the opening/increase of the band gap, and all considered monolayers exhibit semiconducting electronic properties (see Table 3). The halogen atoms' influence on the band gap increasing is more significant than chalcogen and the band gap values range from near-zero values in the case of $Se_2Mo_3Te_2$ to 1.17 eV in the case of $S_2Mo_3F_2$. All Janus Chevrel monolayers except for $O_2Mo_3F_2$ have an indirect band gap, while $O_2Mo_3F_2$ is a direct band gap semiconductor. In all cases, the main contribution to the valence band maximum (VBM) and conduction band minima (CBM) comes from the molybdenum atoms. The features of the monolayer type of the Chevrel phase are that the molybdenum atoms are in a square pyramidal environment making their *d*-orbitals available for interaction with adsorbate molecules, which is useful for catalytic applications. In this case, the replacement of chalcogen atoms by halogen atoms leads to electron density redistribution among the surface Mo atoms since the electronegativity difference makes these Mo atoms attractive to ion sorption. Bader charge analysis of surface Mo atoms (see Table S1) shows similar values of electron deficiency on Mo atoms, which depend on the chalcogen or halogen type and do not depend on its combination in the Janus structure. For example, the Mo atom on the S side has an electron deficiency of 0.89 *e*, which makes this atom attractive for negatively charged ions.
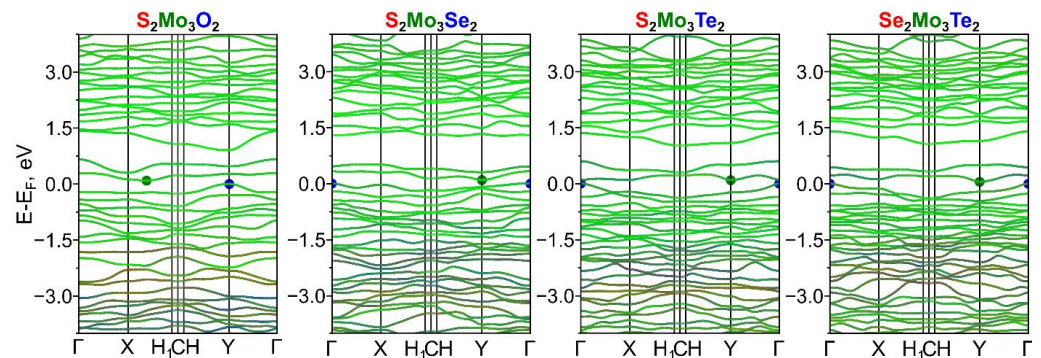
Figure 4. Atom-resolved electronic band structure of dynamically stable Janus $Ch^1_2Mo_3Ch^2_2$ (Ch^1/Ch^2 = O, S, Se, Te) Chevrel phases. The contributions from Ch^1, Ch^2, and Mo atoms are indicated with red, blue, and green colors, respectively.

Table 3. Band gap values (E_g) and vacuum potential difference ($\Delta\Phi$) for opposite sides of dynamically stable Janus $Ch_2Mo_3Hal_2$ and $Ch^1_2Mo_3Ch^2_2$ (Ch^1/Ch^2 = O, S, Se, Te) Chevrel phases.

Monolayer	(001) Surface	(00$\bar{1}$) Surface	E_g, eV	$\Delta\Phi$, eV
$S_2Mo_3Se_2$	Se	S	0.21	0.14
$S_2Mo_3O_2$	O	S	0.10	0.32
$S_2Mo_3Te_2$	Te	S	0.11	0.40
$Se_2Mo_3Te_2$	Te	Se	0.05	0.36
$O_2Mo_3F_2$	F	O	1.05	0.65
$O_2Mo_3Cl_2$	O	Cl	1.10	0.54
$S_2Mo_3F_2$	F	S	1.17	1.17
$S_2Mo_3Cl_2$	Cl	S	1.03	1.41
$S_2Mo_3Br_2$	Br	S	0.89	1.45
$S_2Mo_3I_2$	I	S	0.82	1.51
$Se_2Mo_3Cl_2$	Cl	Se	0.94	1.29
$Se_2Mo_3Br_2$	Br	Se	0.82	1.33
$Se_2Mo_3I_2$	I	Se	0.80	1.41
$Te_2Mo_3Cl_2$	Cl	Te	0.80	1.06
$Te_2Mo_3Br_2$	Br	Te	0.74	1.11
$Te_2Mo_3I_2$	I	Te	0.59	1.20
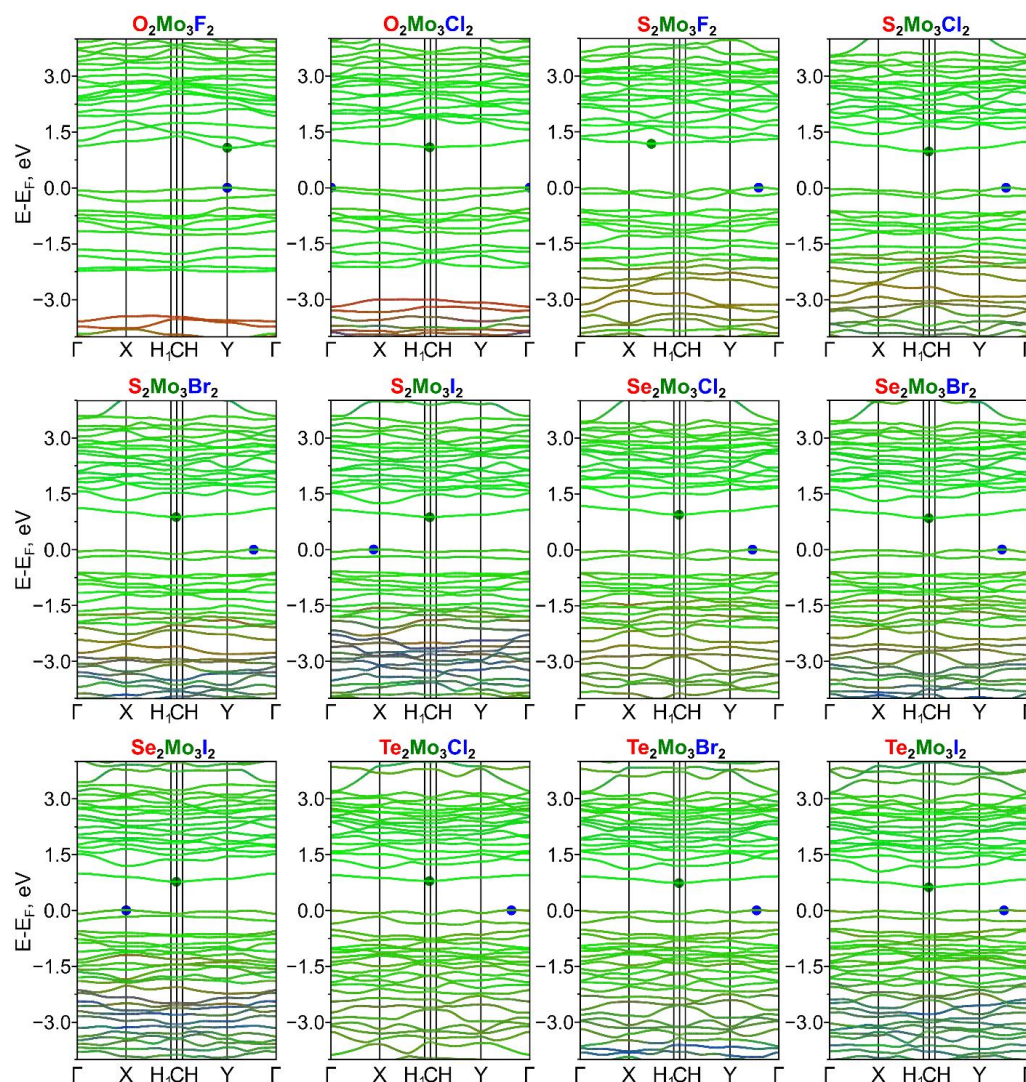
Figure 5. Atom-resolved electronic band structure of dynamically stable Janus $Ch_2Mo_3Hal_2$ (Ch = O, S, Se, Te and Hal = F, Cl, Br, I) Chevrel phases. The contributions from Ch, Hal, and Mo atoms are indicated with red, blue, and green colors, respectively.

To be applied in water-splitting reactions, the CBM of the non-Janus monolayer must be higher than the reduction level of hydrogen, while the VBM must be lower than the oxidation level of oxygen [73], resulting in restriction of the band gap value: $E_g > 1.23$ eV [73]. The feature of Janus monolayers is the presence of two inequivalent surfaces—(001) and $(00\bar{1})$—leading to the appearance of an intrinsic dipole moment, resulting in the electrostatic potential difference between the opposite sides of the monolayers. The intrinsic dipole moment in the Janus monolayer leads to the modification of the restriction on the band gap value:

$$E_g > 1.23 - \Delta\Phi \tag{1}$$

where $\Delta\Phi$ is the difference between the vacuum levels of the opposite sides of Janus monolayers. Additionally, the necessary condition of the photocatalytic water-splitting process is the following: the VBM of the (001) surface must be lower than the oxidation potential, while the CBM of the $(00\bar{1})$ surface must be higher than the reduction potential [73]. It should be noted that in actuality, the redox potentials of water are pH resistant [74].

The band edge positions of dynamically stable $Ch^1_2Mo_3Ch^2_2$ (Ch^1/Ch^2 = O, S, Se, Te) and $Ch_2Mo_3Hal_2$ (Ch = O, S, Se, Te and Hal = F, Cl, Br, I) monolayers, taking into

account the influence of the intrinsic dipole moment concerning the redox potentials of water at pH = 0 and pH = 7, are presented in Figure 6. According to the obtained results, $Ch^1_2Mo_3Ch^2_2$ Janus monolayers do not provide either the reaction of hydrogen production or the reaction of oxygen generation at both considered values of pH; therefore, these structures are not consistent for photocatalytic water splitting.
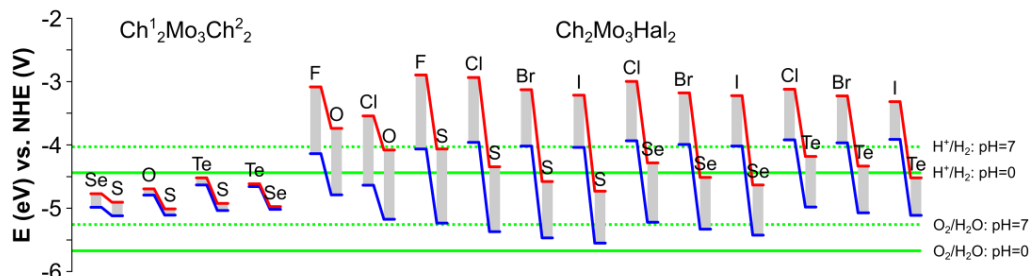
Figure 6. Band edge positions of dynamically stable Janus $Ch^1_2Mo_3Ch^2_2$ and $Ch_2Mo_3Hal_2$ Chevrel monolayer (Ch^1/Ch^2 = O, S, Se, Te; Hal = F, Cl, Br, I) structures compared with the redox potentials of water. The values are given concerning the vacuum level (in eV). The CBM and VBM are marked by red and blue lines. The redox potentials of water are denoted as the green lines for pH = 7 (dashed) and pH = 0 (solid) [74].

Most of the $Ch_2Mo_3Hal_2$ monolayers belong to the type-1 material in neutral and acidic media, according to [75], as this material is suitable for only the HER or the OER due to the band alignments (see Table S2).

Overall water splitting can be achieved for $S_2Mo_3I_2$ in neutral media and $S_2Mo_3Br_2$ in alkali media. A possible way to tune electronic properties is through a variation of halogen content on one side of the Janus monolayer. The replacement of a Br with an S atom ($S_2Mo_3Br_2$) leads to CBM shifting on the halogen side, which makes this material suitable for HER in neutral and acidic media (see Figure S3). However, the reverse side of the coin is that CBM will shift upwards on the chalcogen side.

One more important property of the catalyst material in the case of the photocatalytic process is the ability of the material to absorb the energy of incident solar radiation. To characterize the considered materials, we calculated the optical properties by considering the complex dielectric function $\varepsilon(\lambda) = \varepsilon_1(\lambda) + i\varepsilon_2(\lambda)$, in which the real part $\varepsilon_1(\lambda)$ was calculated using the Kramers–Kronig relation, while the imaginary part $\varepsilon_2(\lambda)$ was determined by the sum of empty states [76,77]. The wavelength-dependent extinction coefficient in the perpendicular direction and parallel to the surface of the monolayer was calculated according to [78] as:

$$K(\lambda) = \left[\frac{\sqrt{\varepsilon_1^2(\lambda) + \varepsilon_2^2(\lambda)} - \varepsilon_1(\lambda)}{2} \right]^{\frac{1}{2}} \qquad (2)$$

The resulting dependences for the Janus monolayers suitable for a catalytic process are presented in Figure 7, while $Ch^1_2Mo_3Ch^2_2$ and Mo_3Ch_4 are presented in Figures S4 and S5, respectively. Overall, Janus Chevrel monolayers suitable for catalysis (Figure 7) are characterized by a strong peak at 250–300 nm in both the transverse direction and perpendicular to the surface, which correspond to the UV region. In the case of oxygen-containing Janus structures, there is also a separate peak at 150–160 nm (UV region) in both the transverse direction and perpendicular to the surface. In the case of Te-containing monolayers, the intensity of the extinction coefficient decreases compared with pristine monolayers (Figure S4), while in other cases, the intensity is comparable. Overall, Janus monolayers can absorb the light at ultraviolet and visible spectral ranges, indicating a high potential for application in photocatalytic water-splitting reactions and as an element of optoelectronic devices.
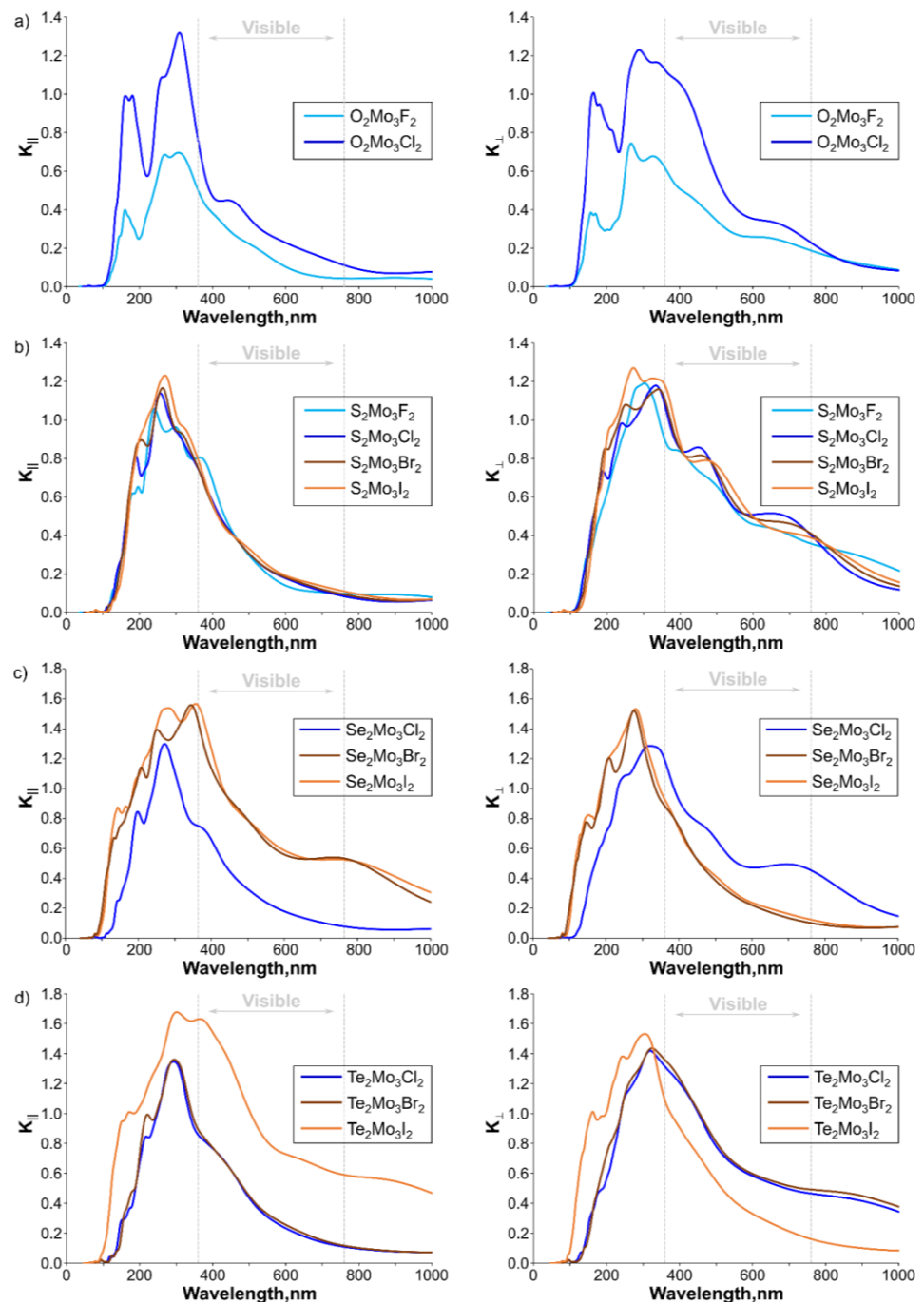
Figure 7. Wavelength dependence of the extinction coefficient in the transverse direction and perpendicular to the surface for dynamically stable Janus $Ch_2Mo_3Hal_2$ Chevrel phases (Ch = O, S, Se, Te; Hal = F, Cl, Br, I): (**a**) oxygen-, (**b**) sulfur-, (**c**) selenium-, and (**d**) tellurium-containing monolayers.

To facilitate the experimental identification of Chevrel monolayers, we simulated vibrational spectra for the initial bulk Mo_6S_8 Chevrel crystal [79] (Figure 8a,b) and the individual Mo_6S_8 monolayer (Figure 8c,d). Experimental Raman spectra of bulk Mo_6S_8 found in [21,80] indicate the existence of two strong sharp peaks in a high-wavenumber region associated with Mo–S stretching vibrations [21]. The same strong peaks were observed in the case of $NiMo_3S_4$ [81]; however, no such peaks were found in the case of $BaMo_6S_8$, $Cu_{1.8}Mo_6S_8$, $Cu_{3.2}Mo_6S_8$, $PbMo_6S_8$, and $SnMo_6S_8$ crystals with a Chevrel structure [82]. In [83], the Raman spectra of $Mo_6S_3I_6$ nanowires are presented in a wide range of temperatures and the existence of such peaks is shown in the case of samples

synthesized at 900 and 1000 °C. At temperatures above 1000 °C, a powder XRD pattern of $Mo_6S_3I_6$ no longer contains lines fitting with MoS_2 and the related bands disappear from the Raman spectra. In Figure 8a, it can be seen that the high-wavenumber region of the simulated spectrum of bulk Mo_6S_8 does not contain these strong bands, but if we consider the combination of bulk Mo_6S_8 and bulk MoS_2 spectra, the resulting figure (Figure 8a) is in good agreement with the experimental data from [21,80]. Thus, we suppose that the samples studied in [21,80,81] can have the impurities of MoS_2. Due to the complexity of the Mo_6S_8 structure, the Raman spectrum obtained in this work theoretically can be assigned based on the phonon density of states calculation (see Figure 8b). The contribution of sulfur ion vibrations is significantly above 250 cm^{-1}. A medium band at 181 cm^{-1} and a strong band at 231 cm^{-1} are associated with Mo translation. The low-wavenumber spectral range contains both Mo and S ion vibrations.

The phonon DOS for the Mo_3S_4 Chevrel monolayer is shown in Figure 8d. Despite the large sulfur phonon density of states in the high-wavenumber region (above 300 cm^{-1}), the Raman intensities in the spectrum shown in Figure 8d are weak. There are no totally symmetric vibrations of the Mo_3S_4 Chevrel monolayer like in the case of MoS_2 [84]. For example, the vibrational mode with the highest wavenumber value (404 cm^{-1}) involves only half of the sulfur ions on each monolayer surface and, at the same time, the sulfur ions remain motionless on the opposite surface (see Figure S6a). Such behavior is similar to the MoSSe Janus monolayers [85]. In this case, the vibration of only one side of the monolayer does not manifest itself as a strong, medium, or even weak Raman band. The strong band at 284 cm^{-1} is associated with in-plane ions' movement, as shown in Figure S6b. The strong spectral band at 210 cm^{-1} can be described as the stretching of a Mo_3S_4 Chevrel-like molecule, as presented in Figure S6c. The strong lines at 141 cm^{-1} (Figure S6d) and 123 cm^{-1} are out-of-plane and in-plane vibrations, respectively. Meanwhile, the spectral lines in Figure 8c above 100 cm^{-1} can be described as the translations of ions, and the contribution of these ions can be determined using Figure 8d. Raman bands below 100 cm^{-1} are assigned as the rotations of Mo_3S_4 Chevrel-like molecules (see Figure S6c).

As a representative of $Ch_2Mo_3Hal_2$ Chevrel monolayers, we considered the $S_2Mo_3Br_2$ monolayer and simulated its Raman spectra as dynamically stable and suitable for the photocatalytic process (Figure 8e). According to the phonon density of states shown in Figure 8f, the vibrations of S and Mo ions contribute to the main intense spectral bands of the $S_2Mo_3Br_2$ Raman spectrum (from 200 to 417 cm^{-1}). Bromine vibrations are in the region below 200 cm^{-1}; however, the calculated intensities of corresponding Raman bands are weak. The low-intensity bands above 350 $^{-1}$cm in the Raman spectrum of $S_2Mo_3Br_2$ are mainly associated with S vibrations, the forms of which are shown in Figure S6f,g. The strongest spectral band in Figure 8e is associated with Mo–S stretching vibrations. The group of spectral bands from 200 to 235 cm^{-1} can be attributed to antisymmetric movements of S ions as, for example, are shown in Figure S6h.

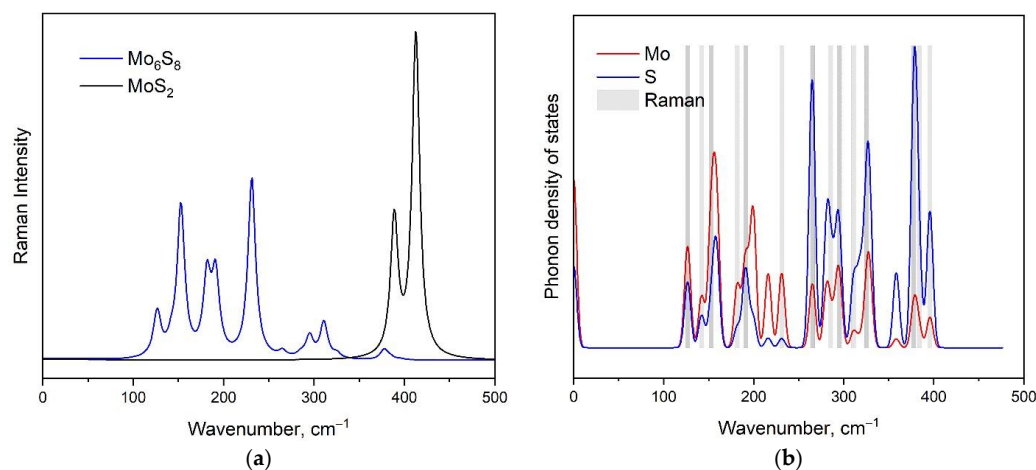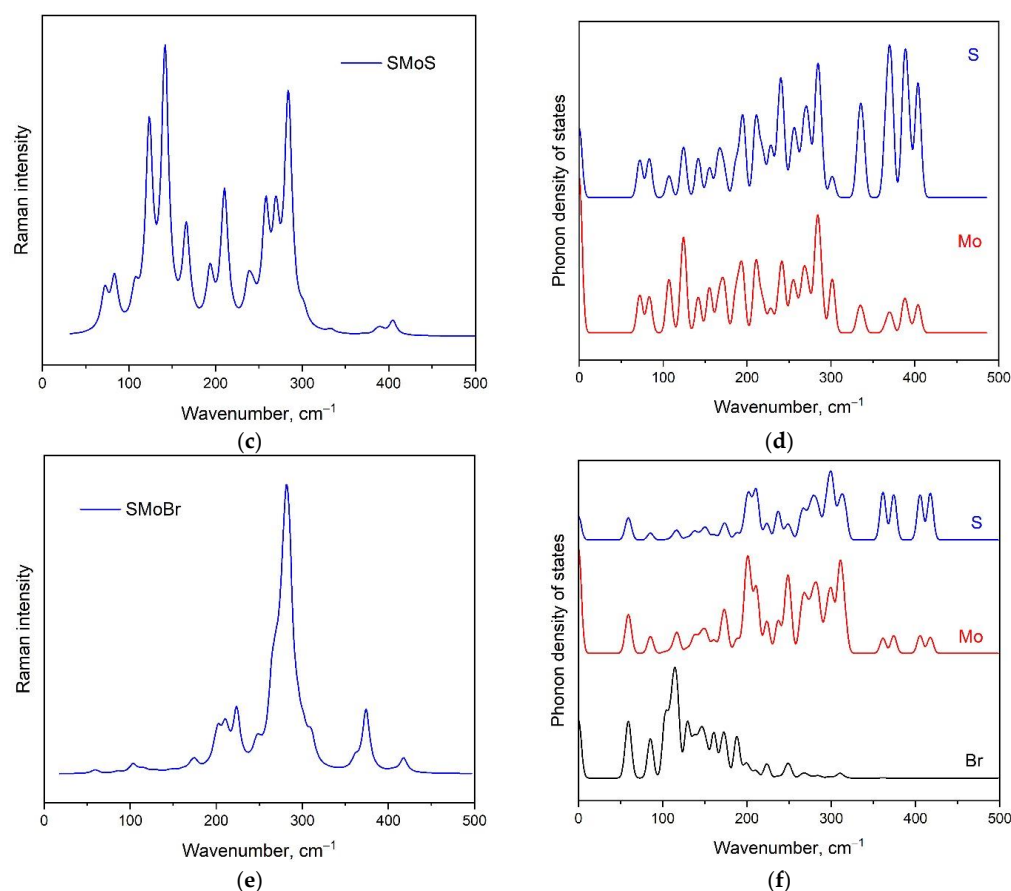**Figure 8.** *Cont.*

Figure 8. Simulated Raman spectra of the Chevrel phase of (**a**) bulk Mo_6S_8 (blue) and MoS_2 (black); (**c**) Mo_3S_4 monolayer; (**e**) $S_2Mo_3Br_2$ monolayer. The corresponding phonon densities of states are shown in (**b**,**d**,**f**), respectively.

4. Conclusions

The photocatalytic water-splitting materials can most likely be found in Janus-type structures consisting of transition metals, chalcogen, and halogen atoms. Here, we theoretically investigated a novel type of Janus structure with the Chevrel phase topology and considered the physical properties and stability. The calculated exfoliation energy from the corresponding bulk chalcogenides demonstrated the possibility of monolayer exfoliation, which can be transformed to suit Janus structures by replacing chalcogen atoms with halogen atoms from one side of the monolayer. The electronic structure calculations demonstrated that halogen doping increases the band gap compared with non-Janus structures, which makes these materials appropriate for the HER and the OER. Among all the considered 2D structures, $S_2Mo_3I_2$ is the most promising candidate for overall water splitting due to the appropriate band alignments relative to the redox potentials of water and the ability to absorb at the UV and visible regions of the light spectra. The calculated Raman spectra can play the role of characteristic blueprints, facilitating the experimental identification and verification of the considered structures. The theoretical results that were obtained open up the prospects for the experimental synthesis and investigation of new compounds based on the Chevrel monolayer phase for photocatalytic as well as for other technological applications.

$Ch_2Mo_3Ch_2$ (Ch = S, Se, Te) Chevrel monolayers; Figure S3. Band edge positions of Janus $(Br_2S_2)Mo_6S_4$, $(Br_3S)Mo_3S_4$ and $(Br_4)Mo_3S_4$ Chevrel monolayers compared with the redox potentials of water. The values are given concerning the vacuum level (in eV); Figure S4. Wavelength dependence of the extinction coefficient in the transverse direction and perpendicular to the surface for Janus $Ch_2Mo_3Ch_2$ (Ch = S, Se, Te) Chevrel phases; Figure S5. Wavelength dependence of the extinction coefficient in the transverse direction and perpendicular to the surface for dynamically stable Janus $Ch^1_2Mo_3Ch^2_2$ (Ch^1/Ch^2 = O, S, Se, Te) Chevrel phases; Figure S6. Vibrational modes in the Mo_3S_4 monolayer at (a) 404 cm^{-1}, (b) 283 cm^{-1}, (c) 210 cm^{-1}, (d) 141 cm^{-1}, and (e) 72 cm^{-1}. Graphical presentation of vibrations in the $S_2Mo_3Br_2$ monolayer at (f) 417 cm^{-1}, (g) 374 cm^{-1}, and (h) 209 cm^{-1}.

References

1. Novoselov, K.S.; Geim, A.K.; Morozov, S.V.; Jiang, D.; Zhang, Y.; Dubonos, S.V.; Grigorieva, I.V.; Firsov, A.A. Electric Field Effect in Atomically Thin Carbon Films. *Science* **2004**, *306*, 666–669. [CrossRef] [PubMed]
2. Balan, A.P.; Puthirath, A.B.; Roy, S.; Costin, G.; Oliveira, E.F.; Saadi, M.; Sreepal, V.; Friedrich, R.; Serles, P.; Biswas, A.; et al. Non-Van Der Waals Quasi-2D Materials; Recent Advances in Synthesis, Emergent Properties and Applications. *Mater. Today* **2022**, *58*, 164–200. [CrossRef]
3. Gibaja, C.; Rodríguez-San-Miguel, D.; Paz, W.S.; Torres, I.; Salagre, E.; Segovia, P.; Michel, E.G.; Assebban, M.; Ares, P.; Hernández-Maldonado, D. Exfoliation of Alpha-Germanium: A Covalent Diamond-Like Structure. *Adv. Mater.* **2021**, *33*, 2006826. [CrossRef] [PubMed]
4. Sun, Y.; Felser, C.; Yan, B. Graphene-Like Dirac States and Quantum Spin Hall Insulators in Square-Octagonal MX_2 (M = Mo, W; X = S, Se, Te) Isomers. *Phys. Rev. B* **2015**, *92*, 165421. [CrossRef]
5. Ma, Y.; Kou, L.; Li, X.; Dai, Y.; Heine, T. Two-Dimensional Transition Metal Dichalcogenides with a Hexagonal Lattice: Room-Temperature Quantum Spin Hall Insulators. *Phys. Rev. B* **2016**, *93*, 035442. [CrossRef]
6. Gavryushkin, P.; Sagatov, N.; Sukhanova, E.; Medrish, I.; Popov, Z. Janus Structures of SMoSe and SVSe Compositions with Low Enthalpy and Unusual Crystal Chemistry. *J. Appl. Crystallogr.* **2022**, *55*, 1324–1335. [CrossRef]
7. Sukhanova, E.V.; Bereznikova, L.A.; Manakhov, A.M.; Al Qahtani, H.S.; Popov, Z.I. A Novel Membrane-like 2D A'-MoS2 as Anode for Lithium- and Sodium-Ion Batteries. *Membranes* **2022**, *12*, 1156. [CrossRef]
8. Sukhanova, E.; Kvashnin, A.; Bereznikova, L.; Zakaryan, H.; Aghamalyan, M.; Kvashnin, D.G.; Popov, Z. 2D-Mo_3S_4 Phase as Promising Contact for MoS_2. *Appl. Surf. Sci.* **2022**, *589*, 152971. [CrossRef]
9. Joseph, T.; Ghorbani-Asl, M.; Kvashnin, A.G.; Larionov, K.V.; Popov, Z.; Sorokin, P.B.; Krasheninnikov, A.V. Nonstoichiometric Phases of Two-Dimensional Transition-Metal Dichalcogenides: From Chalcogen Vacancies to Pure Metal Membranes. *J. Phys. Chem. Lett.* **2019**, *10*, 6492–6498. [CrossRef]
10. Chepkasov, I.V.; Sukhanova, E.V.; Kvashnin, A.G.; Zakaryan, H.A.; Aghamalyan, M.A.; Mamasakhlisov, Y.S.; Manakhov, A.M.; Popov, Z.I.; Kvashnin, D.G. Computational Design of Gas Sensors Based on V3S4 Monolayer. *Nanomaterials* **2022**, *12*, 774. [CrossRef]
11. Sukhanova, E.V.; Kvashnin, A.G.; Agamalyan, M.A.; Zakaryan, H.A.; Popov, Z.I. Map of Two-Dimensional Tungsten Chalcogenide Compounds (W–S, W–Se, W–Te) Based on USPEX Evolutionary Search. *JETP Lett.* **2022**, *115*, 292–296. [CrossRef]
12. Peng, Y.; Zhu, Q.; Xu, W.; Cao, J. High Anisotropic Optoelectronics in Monolayer Binary M_8X_{12} (M = Mo, W; X = S, Se, Te). *ACS Appl. Mater. Interfaces* **2022**, *14*, 27056–27062. [CrossRef] [PubMed]
13. Wang, X.; Guan, X.; Ren, X.; Liu, T.; Huang, W.; Cao, J.; Jin, C. Deriving 2D M_2X_3 (M = Mo, W, X = S, Se) by Periodic Assembly of Chalcogen Vacancy Lines in Their MX2 Counterparts. *Nanoscale* **2020**, *12*, 8285–8293. [CrossRef]
14. Chevrel, R.; Sergent, M.; Prigent, J. Sur de Nouvelles Phases Sulfurées Ternaires Du Molybdène. *J. Solid State Chem.* **1971**, *3*, 515–519. [CrossRef]

15. Singstock, N.R.; Ortiz-Rodríguez, J.C.; Perryman, J.T.; Sutton, C.; Velázquez, J.M.; Musgrave, C.B. Machine Learning Guided Synthesis of Multinary Chevrel Phase Chalcogenides. *J. Am. Chem. Soc.* **2021**, *143*, 9113–9122. [CrossRef]

16. Peña, O. Chevrel Phases: Past, Present and Future. *Phys. C Supercond. Its Appl.* **2015**, *514*, 95–112. [CrossRef]

17. Zhao, W.; Zhang, Y.; Li, H.; Wang, K.; Jiang, K. Large-Scale Fabricating Carbon Coating Chevrel Phase in Molten Salts: Implications for High-Performance Magnesium-Ion Battery Cathode. *J. Alloys Compd.* **2022**, *925*, 166745. [CrossRef]

18. Aurbach, D.; Lu, Z.; Schechter, A.; Gofer, Y.; Gizbar, H.; Turgeman, R.; Cohen, Y.; Moshkovich, M.; Levi, E. Prototype Systems for Rechargeable Magnesium Batteries. *Nature* **2000**, *407*, 724–727. [CrossRef]

19. Geng, L.; Lv, G.; Xing, X.; Guo, J. Reversible Electrochemical Intercalation of Aluminum in Mo_6S_8. *Chem. Mater.* **2015**, *27*, 4926–4929. [CrossRef]

20. Tong, Y.; Gao, A.; Zhang, Q.; Gao, T.; Yue, J.; Meng, F.; Gong, Y.; Xi, S.; Lin, Z.; Mao, M.; et al. Cation-Synergy Stabilizing Anion Redox of Chevrel Phase Mo_6S_8 in Aluminum Ion Battery. *Energy Storage Mater.* **2021**, *37*, 87–93. [CrossRef]

21. Elgendy, A.; Papaderakis, A.A.; Byrne, C.; Sun, Z.; Lauritsen, J.V.; Higgins, E.P.C.; Ejigu, A.; Cernik, R.; Walton, A.S.; Lewis, D.J.; et al. Nanoscale Chevrel-Phase Mo_6S_8 Prepared by a Molecular Precursor Approach for Highly Efficient Electrocatalysis of the Hydrogen Evolution Reaction in Acidic Media. *ACS Appl. Energy Mater.* **2021**, *4*, 13015–13026. [CrossRef]

22. Masschelein, P.; Candolfi, C.; Dauscher, A.; Gendarme, C.; Rabih, A.R.A.O.; Gougeon, P.; Potel, M.; Gall, P.; Gautier, R.; Lenoir, B. Influence of S and Te Substitutions on the Thermoelectric Properties of the Cluster Compound $Ag_{3.8}Mo_9Se_{11}$. *J. Alloys Compd.* **2018**, *739*, 360–367. [CrossRef]

23. Marini, G.; Sanna, A.; Pellegrini, C.; Bersier, C.; Tosatti, E.; Profeta, G. Superconducting Chevrel Phase $PbMo_6S_8$ from First Principles. *Phys. Rev. B* **2021**, *103*, 144507. [CrossRef]

24. Chen, J.; Millis, A.J.; Reichman, D.R. Intermolecular Coupling and Superconductivity in $PbMo_6S_8$ and Other Chevrel Phase Compounds. *Phys. Rev. Mater.* **2018**, *2*, 114801. [CrossRef]

25. Mao, M.; Lin, Z.; Tong, Y.; Yue, J.; Zhao, C.; Lu, J.; Zhang, Q.; Gu, L.; Suo, L.; Hu, Y.-S.; et al. Iodine Vapor Transport-Triggered Preferential Growth of Chevrel Mo_6S_8 Nanosheets for Advanced Multivalent Batteries. *ACS Nano* **2020**, *14*, 1102–1110. [CrossRef] [PubMed]

26. Chevrel, R.; Sergent, M. Chemistry and Structure of Ternary Molybdenum Chalcogenides. In *Superconductivity in Ternary Compounds I: Structural, Electronic, and Lattice Properties*; Fischer, Ø., Maple, M.B., Eds.; Springer: Berlin/Heidelberg, Germany, 1982; pp. 25–86, ISBN 978-3-642-81868-4.

27. Chang, C.L.; Tao, Y.K.; Swinnea, J.S.; Steinfink, H. Oxygen Substitution in Sn and Ni Chevrel Phases. *Acta Crystallogr. Sect. C Cryst. Struct. Commun.* **1987**, *43*, 1461–1465. [CrossRef]

28. Sergent, M.; Fischer, Ø.; Decroux, M.; Perrin, C.; Chevrel, R. Stabilization of Mo_6S_8 by Halogens; New Superconducting Compounds: $Mo_6S_6Br_2$, $Mo_6S_6I_2$. *J. Solid State Chem.* **1977**, *22*, 87–92. [CrossRef]

29. Knöll, R.; Goren, S.; Korn, C.; Shames, A.; Perrin, C.; Privalov, A.; Vieth, H.-M. NMR Study of the Influence of Iodine Substitution in the Chevrel Compounds $Mo_6Te_{8-x}I_x$ and $Mo_6Se_{8-x}I_x$. *Phys. B Condens. Matter* **2002**, *324*, 157–166. [CrossRef]

30. Lin, F.; Fang, Y.; Che, X.; Zhang, S.; Huang, F. Superconductivity in the Electron-Doped Chevrel Phase Compound $Mo_6S_{6.8}Te_{1.2}$. *Inorg. Chem.* **2020**, *59*, 6785–6789. [CrossRef]

31. Zhong, Q.; Dai, Z.; Liu, J.; Zhao, Y.; Meng, S. Phonon Thermal Transport in Janus Single Layer M_2XY (M = Ga; X, Y = S, Se, Te): A Study Based on First-Principles. *Phys. E Low-Dimens. Syst. Nanostructures* **2020**, *115*, 113683. [CrossRef]

32. Yin, W.-J.; Tan, H.-J.; Ding, P.-J.; Wen, B.; Li, X.-B.; Teobaldi, G.; Liu, L.-M. Recent Advances in Low-Dimensional Janus Materials: Theoretical and Simulation Perspectives. *Mater. Adv.* **2021**, *2*, 7543–7558. [CrossRef]

33. Lv, M.-H.; Li, C.-M.; Sun, W.-F. Spin-Orbit Coupling and Spin-Polarized Electronic Structures of Janus Vanadium-Dichalcogenide Monolayers: First-Principles Calculations. *Nanomaterials* **2022**, *12*, 382. [CrossRef] [PubMed]

34. Yang, F.; Shang, J.; Kou, L.; Li, C.; Deng, Z. Mechanical Behaviors in Janus Transition-Metal Dichalcogenides: A Molecular Dynamics Simulation. *Nanomaterials* **2022**, *12*, 1910. [CrossRef] [PubMed]

35. Peng, R.; Ma, Y.; Huang, B.; Dai, Y. Two-Dimensional Janus PtSSe for Photocatalytic Water Splitting under the Visible or Infrared Light. *J. Mater. Chem. A* **2019**, *7*, 603–610. [CrossRef]

36. Ju, L.; Bie, M.; Shang, J.; Tang, X.; Kou, L. Janus Transition Metal Dichalcogenides: A Superior Platform for Photocatalytic Water Splitting. *J. Phys. Mater.* **2020**, *3*, 022004. [CrossRef]

37. Tang, X.; Kou, L. 2D Janus Transition Metal Dichalcogenides: Properties and Applications. *Phys. Status Solidi (B)* **2022**, *259*, 2100562. [CrossRef]

38. Ju, L.; Qin, J.; Shi, L.; Yang, G.; Zhang, J.; Sun, L. Rolling the WSSe Bilayer into Double-Walled Nanotube for the Enhanced Photocatalytic Water-Splitting Performance. *Nanomaterials* **2021**, *11*, 705. [CrossRef]

39. Lin, L.; Hisatomi, T.; Chen, S.; Takata, T.; Domen, K. Visible-Light-Driven Photocatalytic Water Splitting: Recent Progress and Challenges. *Trends Chem.* **2020**, *2*, 813–824. [CrossRef]

40. Feliczak-Guzik, A. Nanomaterials as Photocatalysts—Synthesis and Their Potential Applications. *Materials* **2022**, *16*, 193. [CrossRef]

41. Lu, A.-Y.; Zhu, H.; Xiao, J.; Chuu, C.-P.; Han, Y.; Chiu, M.-H.; Cheng, C.-C.; Yang, C.-W.; Wei, K.-H.; Yang, Y.Y.P.; et al. Janus Monolayers of Transition Metal Dichalcogenides. *Nat. Nanotechnol.* **2017**, *12*, 744–749. [CrossRef]

42. Zhang, J.; Jia, S.; Kholmanov, I.; Dong, L.; Er, D.; Chen, W.; Guo, H.; Jin, Z.; Shenoy, V.B.; Shi, L.; et al. Janus Monolayer Transition-Metal Dichalcogenides. *ACS Nano* **2017**, *11*, 8192–8198. [CrossRef] [PubMed]

43. Yagmurcukardes, M.; Sevik, C.; Peeters, F.M. Electronic, Vibrational, Elastic, and Piezoelectric Properties of Monolayer Janus MoSTe phases: A First-Principles Study. *Phys. Rev. B* **2019**, *100*, 045415. [CrossRef]

44. Wang, Z. 2H→1T′ Phase Transformation in Janus Monolayer MoSSe and MoSTe: An Efficient Hole Injection Contact for 2H-MoS$_2$. *J. Mater. Chem. C* **2018**, *6*, 13000–13005. [CrossRef]

45. Zhang, Y.; Ye, H.; Yu, Z.; Liu, Y.; Li, Y. First-Principles Study of Square Phase MX$_2$ and Janus MXY (M = Mo, W; X, Y = S, Se, Te) Transition Metal Dichalcogenide Monolayers under Biaxial Strain. *Phys. E Low-Dimens. Syst. Nanostructures* **2019**, *110*, 134–139. [CrossRef]

46. Tang, X.; Li, S.; Ma, Y.; Du, A.; Liao, T.; Gu, Y.; Kou, L. Distorted Janus Transition Metal Dichalcogenides: Stable Two-Dimensional Materials with Sizable Band Gap and Ultrahigh Carrier Mobility. *J. Phys. Chem. C* **2018**, *122*, 19153–19160. [CrossRef]

47. Qin, Y.; Sayyad, M.; Montblanch, A.R.; Feuer, M.S.G.; Dey, D.; Blei, M.; Sailus, R.; Kara, D.M.; Shen, Y.; Yang, S.; et al. Reaching the Excitonic Limit in 2D Janus Monolayers by In Situ Deterministic Growth. *Adv. Mater.* **2021**, *34*, 2106222. [CrossRef]

48. Wan, X.; Chen, E.; Yao, J.; Gao, M.; Miao, X.; Wang, S.; Gu, Y.; Xiao, S.; Zhan, R.; Chen, K.; et al. Synthesis and Characterization of Metallic Janus MoSH Monolayer. *ACS Nano* **2021**, *15*, 20319–20331. [CrossRef]

49. Hohenberg, P.; Kohn, W. Inhomogeneous Electron Gas. *Phys. Rev.* **1964**, *136*, B864–B871. [CrossRef]

50. Kohn, W.; Sham, L.J. Self-Consistent Equations Including Exchange and Correlation Effects. *Phys. Rev.* **1965**, *140*, A1133–A1138. [CrossRef]

51. Kresse, G.; Furthmüller, J. Efficient Iterative Schemes for Ab Initio Total-Energy Calculations Using a Plane-Wave Basis Set. *Phys. Rev. B* **1996**, *54*, 11169–11186. [CrossRef]

52. Kresse, G.; Furthmüller, J. Efficiency of Ab-Initio Total Energy Calculations for Metals and Semiconductors Using a Plane-Wave Basis Set. *Comput. Mater. Sci.* **1996**, *6*, 15–50. [CrossRef]

53. Kresse, G.; Hafner, J. Ab Initio Molecular-Dynamics Simulation of the Liquid-Metal-Amorphous-Semiconductor Transition in Germanium. *Phys. Rev. B* **1994**, *49*, 14251–14269. [CrossRef] [PubMed]

54. Perdew, J.P.; Chevary, J.A.; Vosko, S.H.; Jackson, K.A.; Pederson, M.R.; Singh, D.J.; Fiolhais, C. Atoms, Molecules, Solids, and Surfaces: Applications of the Generalized Gradient Approximation for Exchange and Correlation. *Phys. Rev. B* **1992**, *46*, 6671. [CrossRef]

55. Blöchl, P.; Först, C.J.; Schimpl, J. Projector Augmented Wave Method: Ab Initio Molecular Dynamics with Full Wave Functions. *Bull. Mater. Sci.* **1994**, *50*, 17953–17979. [CrossRef]

56. Monkhorst, H.J.; Pack, J.D. Special Points for Brillouin-Zone Integrations. *Phys. Rev. B* **1976**, *13*, 5188. [CrossRef]

57. Togo, A.; Tanaka, I. First Principles Phonon Calculations in Materials Science. *Scr. Mater.* **2015**, *108*, 1–5. [CrossRef]

58. Bader, R.F.W. Atoms in Molecules. *Acc. Chem. Res.* **1985**, *18*, 9–15. [CrossRef]

59. Henkelman, G.; Arnaldsson, A.; Jónsson, H. A Fast and Robust Algorithm for Bader Decomposition of Charge Density. *Comput. Mater. Sci.* **2006**, *36*, 354–360. [CrossRef]

60. Momma, K.; Izumi, F. VESTA 3 for Three-Dimensional Visualization of Crystal, Volumetric and Morphology Data. *J. Appl. Crystallogr.* **2011**, *44*, 1272–1276. [CrossRef]

61. Oreshonkov, A.S. SI: Advances in Density Functional Theory (DFT) Studies of Solids. *Materials* **2022**, *15*, 2099. [CrossRef]

62. Perdew, J.P.; Burke, K.; Ernzerhof, M. Generalized Gradient Approximation Made Simple. *Phys. Rev. Lett.* **1996**, *77*, 3865. [CrossRef] [PubMed]

63. Clark, S.J.; Segall, M.D.; Pickard, C.J.; Hasnip, P.J.; Probert, M.I.J.; Refson, K.; Payne, M.C. First Principles Methods Using CASTEP. *Z. Für Krist. -Cryst. Mater.* **2005**, *220*, 567–570. [CrossRef]

64. Refson, K.; Tulip, P.R.; Clark, S.J. Variational Density-Functional Perturbation Theory for Dielectrics and Lattice Dynamics. *Phys. Rev. B* **2006**, *73*, 155114. [CrossRef]

65. Porezag, D.; Pederson, M.R. Infrared Intensities and Raman-Scattering Activities within Density-Functional Theory. *Phys. Rev. B* **1996**, *54*, 7830–7836. [CrossRef] [PubMed]

66. Jung, J.H.; Park, C.-H.; Ihm, J. A Rigorous Method of Calculating Exfoliation Energies from First Principles. *Nano Lett.* **2018**, *18*, 2759–2765. [CrossRef]

67. Friedrich, R.; Ghorbani-Asl, M.; Curtarolo, S.; Krasheninnikov, A.V. Data-Driven Quest for Two-Dimensional Non-van der Waals Materials. *Nano Lett.* **2022**, *22*, 989–997. [CrossRef]

68. Gu, J.; Zhao, Z.; Huang, J.; Sumpter, B.G.; Chen, Z. MX Anti-MXenes from Non-Van Der Waals Bulks for Electrochemical Applications: The Merit of Metallicity and Active Basal Plane. *ACS Nano* **2021**, *15*, 6233–6242. [CrossRef]

69. Mounet, N.; Gibertini, M.; Schwaller, P.; Campi, D.; Merkys, A.; Marrazzo, A.; Sohier, T.; Castelli, I.E.; Cepellotti, A.; Pizzi, G.; et al. Two-Dimensional Materials from High-Throughput Computational Exfoliation of Experimentally Known Compounds. *Nat. Nanotechnol.* **2018**, *13*, 246–252. [CrossRef]

70. Padilha, A.C.M.; Soares, M.R.S.; Leite, E.R.; Fazzio, A. Theoretical and Experimental Investigation of 2D Hematite. *J. Phys. Chem. C* **2019**, *123*, 16359–16365. [CrossRef]

71. Haga, T.; Fujimoto, Y.; Saito, S. Electronic Structure and Scanning Tunneling Microscopy Images of Heterostructures Consisting of Graphene and Carbon-Doped Hexagonal Boron Nitride Layers. *Phys. Rev. B* **2019**, *100*, 125403. [CrossRef]

72. Vanpoucke, D.E.P.; Brocks, G. Formation of Pt-Induced Ge Atomic Nanowires on Pt/Ge(001): A Density Functional Theory Study. *Phys. Rev. B* **2008**, *77*, 241308. [CrossRef]

73. Li, X.; Li, Z.; Yang, J. Proposed Photosynthesis Method for Producing Hydrogen from Dissociated Water Molecules Using Incident Near-Infrared Light. *Phys. Rev. Lett.* **2014**, *112*, 018301. [CrossRef] [PubMed]

74. Chakrapani, V.; Angus, J.C.; Anderson, A.B.; Wolter, S.D.; Stoner, B.R.; Sumanasekera, G.U. Charge Transfer Equilibria between Diamond and an Aqueous Oxygen Electrochemical Redox Couple. *Science* **2007**, *318*, 1424–1430. [CrossRef]

75. Ersan, F.; Ataca, C. Janus PtX_nY_{2-n} (X, Y = S, Se, Te ; $0 \leq n \leq 2$) Monolayers for Enhanced Photocatalytic Water Splitting. *Phys. Rev. Appl.* **2020**, *13*, 064008. [CrossRef]

76. Gajdoš, M.; Hummer, K.; Kresse, G.; Furthmüller, J.; Bechstedt, F. Linear Optical Properties in the Projector-Augmented Wave Methodology. *Phys. Rev. B* **2006**, *73*, 045112. [CrossRef]

77. Eberlein, T.; Bangert, U.; Nair, R.R.; Jones, R.; Gass, M.; Bleloch, A.L.; Novoselov, K.; Geim, A.; Briddon, P.R. Plasmon Spectroscopy of Free-Standing Graphene Films. *Phys. Rev. B* **2008**, *77*, 233406. [CrossRef]

78. Lalitha, S.; Karazhanov, S.; Ravindran, P.; Senthilarasu, S.; Sathyamoorthy, R.; Janabergenov, J. Electronic Structure, Structural and Optical Properties of Thermally Evaporated CdTe Thin Films. *Phys. B Condens. Matter* **2007**, *387*, 227–238. [CrossRef]

79. Potel, M.; Gougeon, P.; Chevrel, R.; Sergent, M. Labilité Des Cations Dans Les Chalcogénures Ternaires de Molybdène: Voies d'accès à de Nouvelles Synthèses. *Rev. De Chim. Minérale* **1984**, *21*, 509–536.

80. Chu, H.; Pan, J.; Bai, S.; Ma, Y.; Feng, Y.; Wen, Y.; Yang, Y.; Luo, R.; Chen, A. Carbon Coated Chevrel Phase of Mo_6S_8 as Anode Material for Improving Electrochemical Properties of Aqueous Lithium-Ion Batteries. *Electrochim. Acta* **2017**, *258*, 236–240. [CrossRef]

81. Kong, D.; Wang, Y.; Von Lim, Y.; Huang, S.; Zhang, J.; Liu, B.; Chen, T.; Yang, H.Y. 3D Hierarchical Defect-Rich $NiMo_3S_4$ Nanosheet Arrays Grown on Carbon Textiles for High-Performance Sodium-Ion Batteries and Hydrogen Evolution Reaction. *Nano Energy* **2018**, *49*, 460–470. [CrossRef]

82. Holmgren, D.J.; Demers, R.T.; Klein, M.V.; Ginsberg, D.M. Raman Study of Phonons in Chevrel-Phase Crystals. *Phys. Rev. B* **1987**, *36*, 1952–1955. [CrossRef] [PubMed]

83. Kang, G.-S.; Hu, Q.; Li, S.; Bhoraskar, S.V.; Yoo, J.-B. Synthesis of Novel 1—Dimensional Structure from Mo_6S_8 Chevrel Phase of Electrode for Mg Batteries. *Mater. Res. Express* **2022**, *9*, 085502. [CrossRef]

84. Yao, Y.; Ao, K.; Lv, P.; Wei, Q. MoS_2 Coexisting in 1T and 2H Phases Synthesized by Common Hydrothermal Method for Hydrogen Evolution Reaction. *Nanomaterials* **2019**, *9*, 844. [CrossRef] [PubMed]

85. Oreshonkov, A.S.; Sukhanova, E.V.; Popov, Z.I. Raman Spectroscopy of Janus MoSSe Monolayer Polymorph Modifications Using Density Functional Theory. *Materials* **2022**, *15*, 3988. [CrossRef] [PubMed]